

Efficient Line-by-Line Calculation of Absorption Coefficients to High Numerical Accuracy

April 19, 1996

Lawrence Sparks

Jet Propulsion Laboratory

California Institute of Technology

Pasadena, California

Table Of Contents

1.	Introduction	3
2.	The method of approximation	5
3.	Lorentz profile.....	7
4.	Doppler profile	9
5.	Voigt profile	0
6.	Implementation of the algorithm.....	0
7.	Accuracy	1
8.	Line Rejection	4
9.	Efficiency	17
10.	Discussion	24
11.	Conclusion	25
	Acknowledgments	27
	References	27
	Appendix	29

Abstract

A simple yet efficient method is presented for calculating spectral absorption coefficients to high numerical accuracy. The accuracy achieved is independent of the sampling interval. The method is applicable to any analytic model of the spectral line shape.

1. introduction

To model the transfer of radiation through the atmosphere at high spectral resolution, it is necessary to evaluate contributions to thermal emission and radiative absorption on a line-by-line basis. The accuracy of such radiative transfer calculations depends, in part, on the analytic model chosen to define spectral absorption coefficients and on the numerical accuracy with which this model is evaluated. In practice calculating absorption coefficients proves to be the dominant computational expense of a line-by-line radiative transfer model.

The numerical accuracy to which absorption coefficients should be calculated depends upon the problem at hand, and it proves advantageous if the method of their calculation permits the user to adjust readily the level of accuracy that may be achieved. High accuracy is desirable, for example, when constructing reference tables of absorption coefficients such as those required for interpolation in fast parameterized forward models designed for operational satellite remote sounding [Turner, 1995]. On the other hand, the ability to trade numerical accuracy for speed can prove useful in contexts where absorption coefficients of high numerical accuracy are not required, as warranted, for example, by the size of the experimental error or the magnitude of other systematic errors in the radiative transfer model.

High accuracy is particularly useful in error analysis. A rigorous analysis of the error in retrieved atmospheric profiles, for example, demands that the accuracy of the forward model be quantifiable [Rodgers, 1990]. One may accurately quantify the numerical error due to approximating absorption coefficients by comparing computed radiances with those of the same spectrum calculated using absorption coefficients of high numerical accuracy. In this manner, convergence studies, which are initially useful for validating the implementation of the forward model, can provide a means of determining the numerical error in computed spectra as a function of a user-specified error limit for absorption coefficients. By reducing this error limit, it can be determined, for example, whether an apparent anomaly in a computed spectrum is simply an artifact of approximating the analytic line shape model too crudely. Sensitivity studies can, in turn, assess the dependence of retrieved profiles on the magnitude of the numerical error in the computed absorption coefficients.

Evaluation of spectral absorption coefficients in the infra-red is computationally expensive for three reasons: (1) hundreds of thousands of vibrational and rotational transitions contribute to absorption; (2) each transition defines a spectral line that can contribute to absorption over a wide range of frequency, and (3) absorption coefficients must be sampled at a frequency interval that is sufficiently small to resolve the thinnest lines of interest. For example, the half-width at half-maximum of a spectral line in the stratosphere, where Doppler broadening dominates, is typically 0.001 cm^{-1} . Resolving such lines on a grid of discrete frequencies requires a sampling rate of more than 1000 points per cm^{-1} . On the other hand, collisional broadening in the troposphere typically

produces spectral lines with half-widths at half-maximum of 0.1 cm^{-1} and wings that can span many tens of cm^{-1} . Thus, the direct evaluation of a tropospheric line over, say, 50 cm^{-1} at a sampling interval of 1000 points per cm^{-1} requires evaluation of the model line profile at 50,000 points. When such a calculation is repeated for thousands of lines (there are over 709,000 lines represented in the 1992 HITRAN database [Rothman *et al.*, 1992]) the computational cost quickly becomes prohibitive.

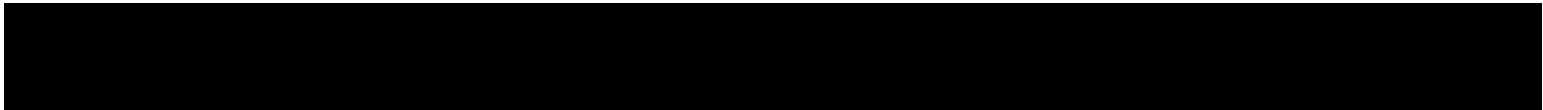
Various strategies have been employed to reduce this computational workload [Drayson, 1966; Kunde and Maguire, 1974; Scott, 1974; Susskind and Scarf, 1978; Clough and Kneizys, 1979; Edwards, 1988; Uchiyama, 1992; Fomin, 1995]. It is common to approach the problem by using multiple frequency grids: fine grids are used to model a line shape near the line center frequency while grids with coarse frequency spacing are used to model the wings. Furthermore, the wings of spectral lines are usually neglected at distances sufficiently far from line center, and a line is neglected altogether if its intensity at line center is sufficiently weak.

These cost-saving strategies are sources of numerical error. For example, interpolation from coarse to fine grids introduces error into the computed absorption coefficients, and the magnitude of this error depends on the size of the interpolation sampling interval. Neglecting lines, or their far wings, is a second source of numerical error: a large number of neglected, small terms can sum to a correction in the magnitude of a given absorption coefficient which is non-negligible, depending upon the degree of accuracy sought.

This paper presents a simple yet efficient method for calculating spectral absorption coefficients to arbitrarily high numerical accuracy. To be more precise, the method provides an efficient means of approximating the contribution of each absorption coefficient of every spectral line retained in the observational model, such that the difference between the approximate coefficient and its exact value (as calculated by the computationally intensive process of summing all line contributions directly) can be rendered arbitrarily small. The method is not dependent upon any particular choice of analytic model for the spectral line shape. Furthermore, the numerical error is independent of the interval with which the spectrum is sampled.

Rather than summing directly the contribution of each line to absorption at each spectral grid point, this method relies on establishing for each line the set of frequencies at which the difference between the analytic value of such a contribution and its interpolated approximation exceeds a limiting small value; the line profile is evaluated only at these frequencies. At each spectral grid point, the differences are summed over all lines. The frequencies at which each line profile is evaluated are determined dynamically: the spacing between such points increases continuously with distance from line center; narrow lines are evaluated on a finer scale than broad lines of the same intensity; and lines of stronger intensity are generally evaluated at more points than those of weaker intensity. It should be emphasized that the wings of spectral lines are not truncated in this method, *i.e.*, every spectral line included in the calculation contributes to absorption over the entire frequency range of interest.

A line-by-line algorithm based on this method of calculating absorption coefficients has been implemented in the forward model of SEASCRAPE (Sequential Evaluation Algorithm for Simultaneous and Concurrent Retrieval of Atmospheric Parameter Estimates), a research code designed to retrieve atmospheric profiles from both nadir and limb measurements of spectral radiation [Sparks *et al.*, 1996]. SEASCRAPE



requires the user to impose an upper limit at runtime on the numerical error permitted in the approximation of absorption coefficients. The user may adjust this limit by orders of magnitude according to the desired level of numerical accuracy.

The method of approximating spectral absorption coefficients is described in Section 2. Application of this method using three distinct models for the line shape, the Lorentz profile, the Doppler profile, and the Voigt profile, is discussed in Sections 3, 4, and 5, respectively. Section 6 provides details concerning the implementation of this method in SEASCRAPE. In Section 7 the accuracy of the method is demonstrated, and an example of a convergence study is provided, in Section 8 this method is studied in relation to the error due to rejection of weak lines from the radiative transfer model. Section 9 addresses the issue of computational efficiency, and the performance of the method is compared to that of LBLRTM [Clough, 1993], a version of FASCOD [Smith *et al.*, 1978, Clough *et al.*, 1981]. A general discussion of various features of the method follows in Section 10, and concluding remarks are presented in Section 11.

2. The method of approximation

Let $\sigma_{s,\ell}(\nu)$, in units of cm^{-1} , represent the contribution of a single spectral line to absorption per unit length at a frequency ν (in cm^{-1}):

$$\sigma_{s,\ell}(\nu) \equiv N_s S_\ell f_\ell(\nu, \nu_\ell) \quad (1)$$

where N_s (in molecules/ cm^{-3}) is the number density of the molecular species to which the spectral line belongs, S_ℓ (in $\text{cm}^{-1}/\text{molecules} \rightarrow \text{cm}^{-2}$) is the line intensity, ν_ℓ (in cm^{-1}) is the unperturbed frequency of the transition, and $f_\ell(\nu, \nu_\ell)$ (in $1/\text{cm}^{-1}$) is the line shape factor [Goody and Yung, 1989]. The line shape factor is normalized such that

$$\int_0^\infty f_\ell(\nu, \nu_\ell) d\nu = 1. \quad (2)$$

Let $\sigma(\nu)$ represent the spectral absorption coefficient at frequency ν , such that

$$\sigma(\nu) \equiv \sum_{s,\ell} \sigma_{s,\ell}(\nu), \quad (3)$$

where the summation is over all the spectral lines of all the molecular species present in the atmosphere.

To establish the method of approximation, the frequency range over which absorption coefficients are to be calculated is divided into 2^M uniform intervals, where M is an integer sufficiently large to ensure that the width of each interval is less than a limiting value, $\delta\nu_{\max}$, specified by the user (the magnitude of $\delta\nu_{\max}$ will not affect the accuracy of the computed absorption coefficients). The frequencies that comprise the boundaries of these intervals are used to define a sequence of frequency grids, each of which is designated a *tier* of the original frequency grid (see Fig. 1). The *base tier* includes the endpoints of the frequency range. Each succeeding (*i.e.*, *higher*) tier consists of the frequencies that lie at the midpoints of the intervals bounded by the frequencies

residing on all lower tiers. The calculation of absorption Coefficients will proceed on a tier-by-tier basis.

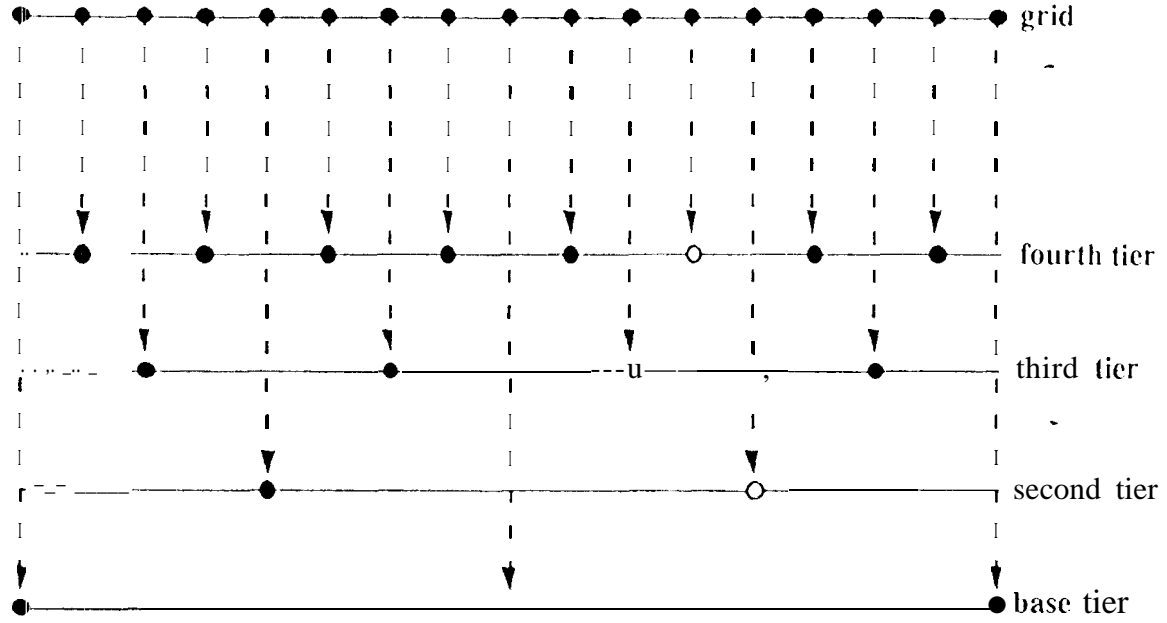


Figure 1. Tiers of the model frequency grid, as defined when using three-point Lagrangian interpolation. The top row represents the frequencies at which monochromatic radiances are to be calculated; the lower rows show the manner in which these frequencies are distributed to form a sequence of grids with successively finer grid spacing. A function evaluated at the open circle on the fourth tier can be approximated by interpolating the function at the open circles on the base, second, and third tiers.

For a frequency ν residing on a given tier above the base tier, the interpolated approximation $\tilde{f}_t(\nu, \nu_t)$ of $f_t(\nu, \nu_t)$ is defined as a linear combination of the values of $f_t(\nu', \nu_t)$ evaluated at the neighboring, frequencies ν' nearest to ν that reside on lower tiers. Let $\tilde{\sigma}_{s,t}(\nu)$ represent the corresponding interpolated approximation of $\sigma_{s,t}(\nu)$, and define, $\tilde{\sigma}(\nu)$ such that

$$\tilde{\sigma}(\nu) \equiv \sum_{s,t} \tilde{\sigma}_{s,t}(\nu). \quad (4)$$

Equations (3) and (4) may be combined to form:

$$\sigma(\nu) \approx \tilde{\sigma}(\nu) + \sum_{s,t} [\sigma_{s,t}(\nu) - \tilde{\sigma}_{s,t}(\nu)]. \quad (5)$$

We can expect the summand in this equation to be negligible (1) when the interpolation sampling interval is sufficiently fine or (2) when ν is sufficiently far from the line center

frequency. The key to the algorithm will be to determine the frequencies on each tier at which this summand is negligible *without* evaluating it at these frequencies.

Spectral absorption coefficients $\sigma(v)$ are calculated starting on the base tier and moving progressively to tiers of finer spacing; eq. (3) is used at frequencies on the base tier, and eq. (5) is used elsewhere. Note that by using an interpolation scheme with constant coefficients (*i. e.*, Lagrangian interpolation), $\bar{\sigma}(v)$ can be calculated as a linear combination of $\sigma(v')$'s evaluated previously at frequencies on tiers below that of v . Computational efficiency is achieved by ignoring those terms in eq. (5) such that

$$|\sigma_{s,\ell}(v) - \bar{\sigma}_{s,\ell}(v)| < \sigma_A, \quad (6)$$

where the accuracy coefficient σ_A is a user-specified, small value. How to determine the frequencies on each tier at which condition (6) is satisfied without evaluating $\sigma_{s,\ell}(v) - \bar{\sigma}_{s,\ell}(v)$ at these frequencies is best illustrated by considering examples.

3. Lorentz profile

In the lower atmosphere, the shape of spectral lines is dominated by collisional broadening, which can be represented most simply by the Lorentz line shape [Goody and Yung, 1989]:

$$f_{L,\ell}(v, v_\ell) = \frac{\alpha_{L,\ell}}{\pi \left[(v - v_\ell)^2 + \alpha_{L,\ell}^2 \right]}, \quad (7)$$

where $\alpha_{L,\ell}$ is the Lorentz half-width at half-maximum of the line. This can be expressed as

$$f_{L,\ell}(v, v_\ell) = \frac{1}{\alpha_{L,\ell} \pi} g\left(\frac{v - v_\ell}{\alpha_{L,\ell}}\right), \quad (8)$$

where

$$g(z) = \frac{1}{z^2 + 1} \quad (9)$$

is independent of spectral line.

To approximate $g(z)$, we shall use three-point Lagrangian interpolation:

$$g(z_0 + p\Delta z) \approx \frac{1}{2} p(p-1)g(z_0 - \Delta z) + (1-p^2)g(z_0) + \frac{1}{2} p(p+1)g(z_0 + \Delta z), \quad (10)$$

or, setting $z = z_0 + p\Delta z$,

$$g(z) \approx \frac{1}{2} p(p+1)g(z - p\Delta z - \Delta z) + (1 - p^2)g(z - p\Delta z) + \frac{1}{2} p(p+1)g(z - p\Delta z + \Delta z) \quad (11)$$

$$\equiv \bar{g}_p(z, \Delta z).$$

We assign indices to the grid points of each tier, with the index of the first point equal to zero, and set $p = 1/2$ and $-1/2$ for grid points with even and odd numbered indices, respectively. Using eqs. (1), (8), (9), and (11), condition (6) can be expressed as

$$\frac{N_s S_\ell}{\alpha_{L,\ell} \pi} \delta g_p \left(\frac{v - v_\ell}{\alpha_{L,\ell}}, \frac{\Delta v}{\alpha_{L,\ell}} \right) < \sigma_A, \quad (12)$$

where

$$\delta g_p(z, \Delta z) \equiv |g(z) - \bar{g}_p(z, \Delta z)|, \quad (13)$$

and Δv is the frequency spacing of the tier on which v lies. The behavior of $\delta g_p(z, \Delta z)$ is discussed in the Appendix.

Place Contours figure here

Figure 2, Contours of $\log_{10} \left(\text{Max}_{-1 \leq p \leq 1} \delta g_p(z, \Delta z) \right)$ on a plane with coordinates $\log_{10} \Delta z$ and $\log_{10} |z / \Delta z|$.

The problem now is to identify on each tier the frequencies at which condition (12) is violated for a given line. In Fig. 2 we have displayed contours of $\log_{10} \left(\text{Max}_{-1 \leq p \leq 1} \delta g_p(z, \Delta z) \right)$ on a plane with coordinates $\log_{10} \Delta z$ and $\log_{10} |z / \Delta z|$ (note that $\Delta z = \Delta v / \alpha_{L,\ell}$ may be interpreted as the frequency spacing in units of Lorentz half-width $\alpha_{L,\ell}$ and that $|z / \Delta z| = -|v - v_\ell| / \Delta v$ may be interpreted as distance from line center in units of frequency spacing Δv). For $\Delta z \ll |z|$, we find that the contours consist of two sets of nearly parallel lines separated by a chain of islands occurring at $\log_{10} |z / \Delta z| \approx -\log_{10} |\Delta z|$, i.e., $|z| \approx 1$. The contour identified by the value $\log_{10} (\sigma_A \alpha_{L,\ell} \pi / N_s S_\ell)$ determines the domain of frequencies for which condition (12) is violated. Note that this contour is bounded from below by a limiting value $\Delta z_{A,\ell}$. "1"bus, the contribution of this line to the summation in eq. (5) can be neglected at frequency grid points residing on each tier with sufficiently fine grid spacing, i.e., $\Delta v < \alpha_{L,\ell} \Delta z_{A,\ell}$. For each tier with $\Delta v \geq \alpha_{L,\ell} \Delta z_{A,\ell}$, the contour intersects $\Delta z = \Delta v / \alpha_{L,\ell}$ at a limiting value $|z / \Delta z| = \xi_{L,A}(\Delta v, \alpha_{L,\ell})$ such that condition (12) is satisfied for frequency grid points that lie sufficiently far from line center; i.e., the contribution of this line to the summation in eq. (5) can also be neglected

at frequency grid points such that $|v - v_l| / \Delta v > \xi_{l,A}(\Delta v, \alpha_{l,A})$. We shall refer to $\xi_{l,A}(\Delta v, \alpha_{l,A})$ as the Lorentz cutoff for the tier with frequency spacing Δv . Knowledge of the Lorentz cutoff for each tier constitutes a solution to the problem.

4. Doppler profile

At high altitudes, the shape of spectral lines is governed by Doppler broadening due to the velocity distribution of the absorbing molecules relative to the observing instrument. The corresponding line shape factor is [Goody and Yung, 1989]

$$f_{D,s,t}(v, v_l) \equiv \frac{1}{\alpha_{D,s,t} \sqrt{\pi}} \exp \left[- \frac{(v - v_l)^2}{\alpha_{D,s,t}^2} \right], \quad (14)$$

where

$$\alpha_{D,s,t} \equiv \frac{v_l}{c} \left(\frac{2k_B T}{m_s} \right)^{1/2} \quad (15)$$

is the Doppler half-width at e^{-1} of the maximum of the profile (rather than 2^{-1} of the maximum as in the definition of $\alpha_{L,t}$), c is the speed of light, k_B is Boltzmann's constant, T is temperature, and m_s is the molecular mass of the absorbing species. This can be expressed as

$$f_{D,s,t}(v, v_l) \equiv \frac{1}{\alpha_{D,s,t} \sqrt{\pi}} g \left(\frac{v - v_l}{\alpha_{D,s,t}} \right), \quad (16)$$

where $g(z)$, now redefined as

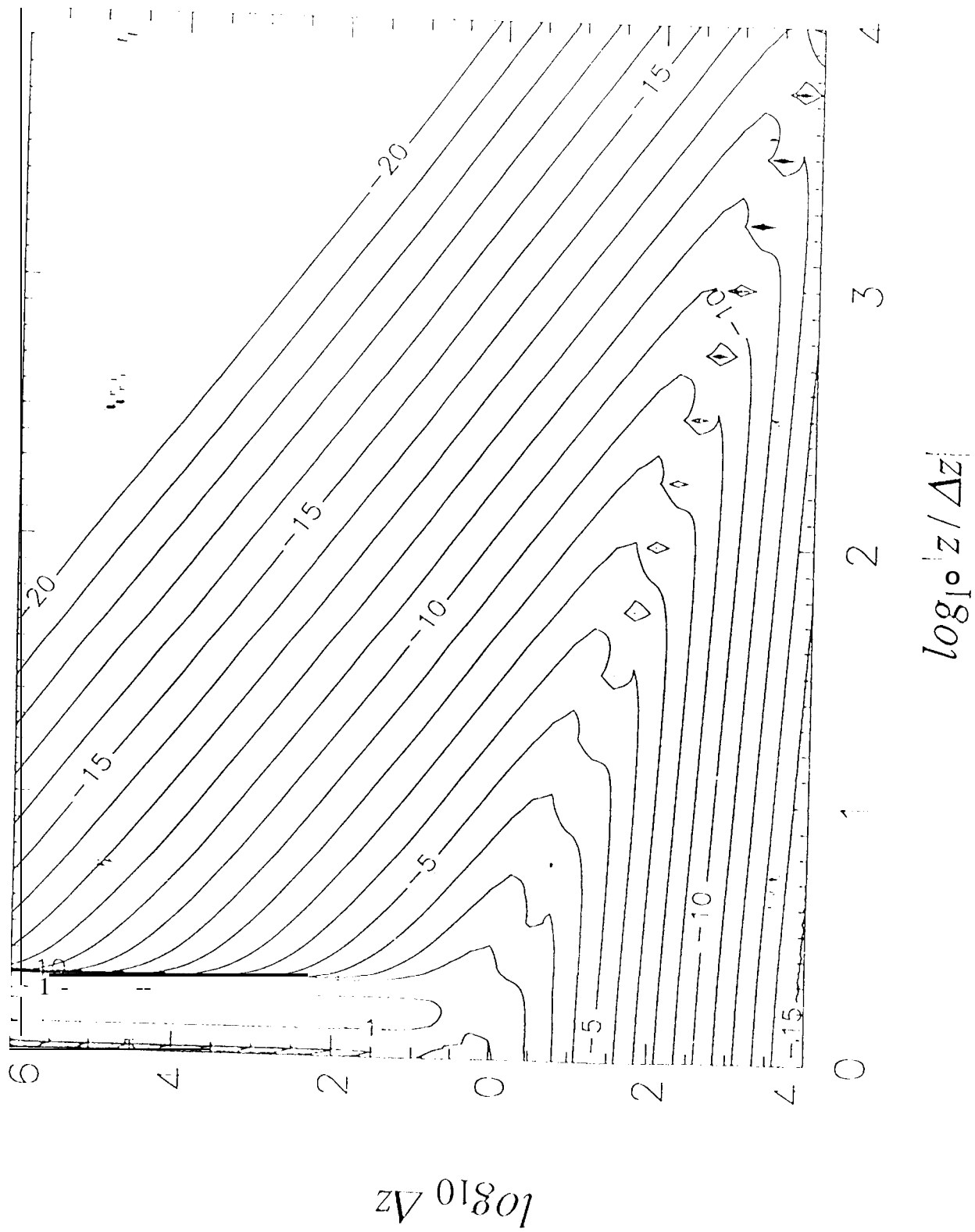
$$g(z) \equiv \exp(-z^2), \quad (17)$$

remains independent of spectral line. As $|v - v_l|$ increases, the magnitude of the Doppler line shape decreases much more rapidly than the magnitude of the Lorentz line shape and effectively vanishes for values of $|v - v_l|$ greater than a few Doppler half-widths.

The analog of condition (12) for the Doppler profile can be expressed as

$$\frac{N_s S_l}{\alpha_{D,s,t} \sqrt{\pi}} \delta g_p \left(\frac{w - v_l}{\alpha_{D,s,t}}, \frac{\Delta v}{\alpha_{D,s,t}} \right) < \sigma_A, \quad (18)$$

where $\delta g_p(z, \Delta z)$ is defined by eq. (13) using eqs. (11) and (17). To determine on each tier the frequencies at which this condition is satisfied, one could follow the procedure used in the previous section. It is sufficient here, however, simply to note that, for



$|z| > 3\Delta z/2$ and $p = \pm 1/2$, $\delta g_p(z, \Delta z) < g(|z| - 3\Delta z/2)$. Thus, condition (18) will be satisfied provided

$$g\left(\frac{|v - v_t|}{\alpha_{D,s,t}} - \frac{3\Delta v}{2\alpha_{D,s,t}}\right) < \frac{\sigma_A \alpha_{D,s,t} \sqrt{\pi}}{N_s S_t} \quad (19)$$

Defining the Doppler cutoff for the tier with frequency spacing Δv as

$$\xi_{D,A}(\Delta v, \alpha_{D,s,t}) \equiv \frac{3}{2} + \frac{\alpha_{D,s,t}}{\Delta v} \left(-\log \frac{\sigma_A \alpha_{D,s,t} \sqrt{\pi}}{N_s S_t} \right)^{1/2}, \quad (20)$$

condition (19) reduces to $|v - v_t|/\Delta v > \xi_{D,A}(\Delta v, \alpha_{D,s,t})$, which is a simpler criterion, though somewhat less restrictive than condition (6), for neglecting terms in the summation of eq. (5).

5. Voigt profile

At intermediate altitudes, both collisional broadening and Doppler broadening are important and can be modeled using the Voigt profile, a convolution of the Lorentz and Doppler profiles [Armstrong, 1967]:

$$f_{v,t}(v, v_t) \equiv \frac{1}{\alpha_{D,s,t} \sqrt{\pi}} V\left(\frac{v - v_t}{\alpha_{D,s,t}}, \frac{\alpha_{L,t}}{\alpha_{D,s,t}}\right), \quad (21)$$

where the Voigt function

$$V(x, y) \equiv \frac{y}{\pi} \int_{-\infty}^{\infty} \frac{e^{-t^2}}{(x - t)^2 + y^2} dt \quad (22)$$

is the real part of the complex probability function. The Voigt line shape reduces to the Lorentz and Doppler line shapes, respectively, in the appropriate limits. On a given tier, condition (6) will be approximately satisfied for values of $|v - v_t|/\Delta v$ that exceed both the Lorentz and the Doppler cutoffs.

6. Implementation of the algorithm

In the implementation of the algorithm described in Section 2 within the forward model of SEASCRAPE, the line strength S_t at temperature T is calculated in terms of the line strength S_{t0} at a reference temperature T_0 as follows:

$$S_t \equiv S_{t0} \frac{Q(T_0)}{Q(T)} \exp\left(-\frac{E_t''}{k_B T_0} + \frac{E_t''}{k_B T}\right) \frac{1 - \exp(-hc v_t / k_B T)}{1 - \exp(-hc v_t / k_B T_0)}, \quad (23)$$

where $Q(T)$ is the total internal partition function and E_l'' is the energy of the lower state of the transition. The line parameters are obtained from the HITRAN molecular database [Rothman *et al.*, 1992].

'1'0 represent the line shape, the forward model uses the Voigt profile, eq. (21). Since the integral in eq. (22) cannot be evaluated in closed form, it must be calculated numerically. Many algorithms have been proposed for approximating the Voigt function, involving various tradeoffs between accuracy and speed (see the review by Schreier [1992]). We have implemented in SEASCRAPPE a version of the Humlicek algorithm [1982], which involves dividing the x - y plane into four domains where ratios of polynomials are used to achieve a relative accuracy that is everywhere better than 1 part in 10^4 . In addition we have introduced the option of using interpolation tables to evaluate the Voigt function in the region $|x|+y < 5.5$ (values of the Voigt function are tabulated on an x - y grid which is sufficiently fine to preserve the relative accuracy of 1 part in 104). The implementation has been coded in C, using real rather than complex arithmetic. All floating-point arithmetic here (as well as throughout SEASCRAPPE) is performed in double precision.

From the data displayed in Fig. 2, we have constructed a table of Lorentz cutoffs over a range of Az and a range of ϵ , where $\log_{10} \epsilon$ identifies a contour in that figure. For a given line and a given tier, we can evaluate $Az = \Delta v / \alpha_{L,t}$ and $\epsilon = \sigma_A \alpha_{L,t} \pi / N_s S_t$, and then use this table to define the corresponding Lorentz cutoff $\xi_{s,t}(Av, \alpha_{L,t})$. When the tier grid spacing Δv is sufficiently fine, the Lorentz cutoff will be zero, and the contribution of the line to the summation in eq. (5) is neglected at all frequency grid points on this and higher tiers. When the cutoff is non-zero, the contribution of the line to the summation in eq. (5) is neglected at frequency grid points on this tier where $|v - v_l| / \Delta v$ is greater than both the Lorentz and the Doppler cutoffs.

When using a line shape model other than those discussed in Sections 3, 4, and 5, one must take care that the conditions

$$\begin{aligned} v_{\max,t} &\geq v_{\max,t-1} + \Delta v_t \\ v_{\min,t-1} &\leq v_{\min,t} + \Delta v_t \end{aligned} \quad (24)$$

are satisfied, where $v_{\max,t}$ and $v_{\min,t}$ are, respectively, the maximum and minimum frequencies, on tier t , of the terms retained in the summation of eq. (5). These conditions ensure that calculation of $\bar{\sigma}_{s,t}(v_{\max,t})$ and $\bar{\sigma}_{s,t}(v_{\min,t})$ will be preceded, on the tiers below tier t , by calculation of each of the values of $0_{s,t}(V)$ required for their evaluation. It can be shown that conditions (24) are satisfied when $v_{\max,t}$ and $v_{\min,t}$ are specified according to either the Lorentz or Doppler cutoffs as defined in Sections 3 and 4 (or the greater of the two as in Section 5).

7. Accuracy

To demonstrate the method of approximation presented in Section 2, we have defined a benchmark similar to one that has been used to compare, in various computational environments, the performance of LBLRTM [Clough, 1993], a derivative

version of FASCODE [Smith *et al.*, 1978, Clough *et al.*, 1981]. The benchmark consists of a spectrum in the CO₂ band between 650 and 800 cm⁻¹ as viewed in nadir from a height of 19.67 km (see Fig. 3). Emission from the ground is modeled as a black body

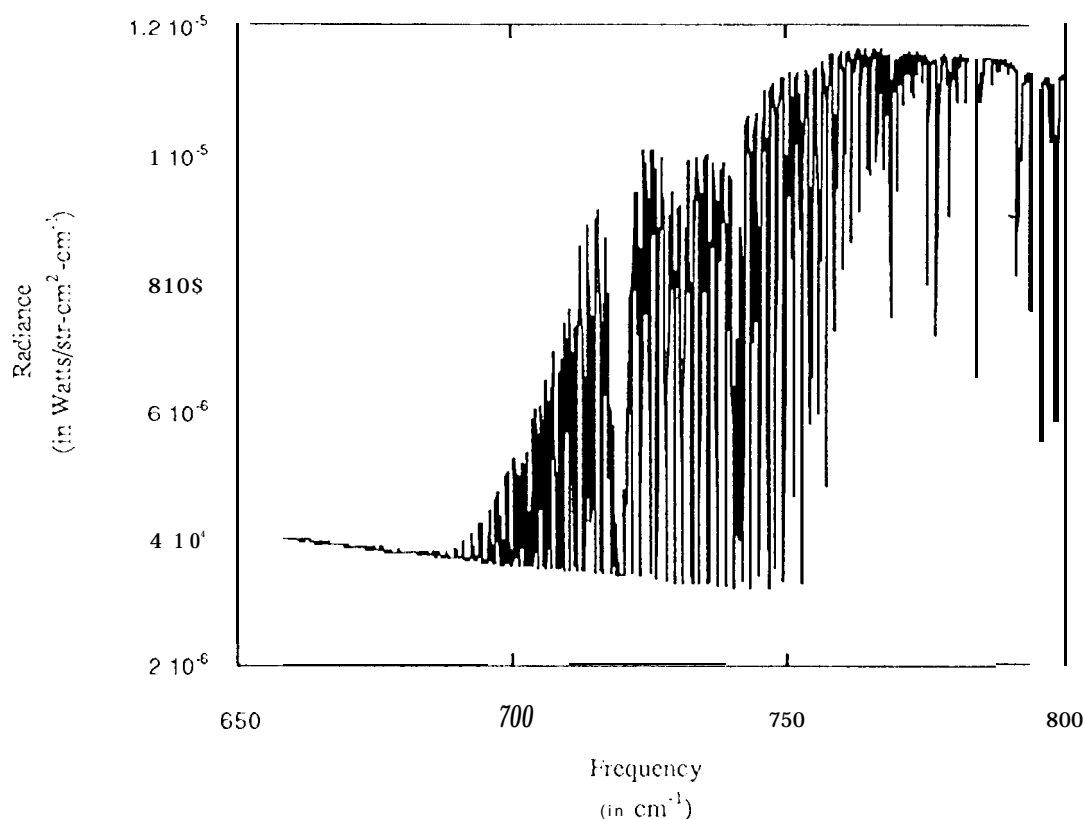


Figure 3. Benchmark spectrum consisting, of radiances (in Watts/str-cm²-cm⁻¹) in the CO₂ band from 650 to 800 cm⁻¹.

(i.e., the surface emissivity is equal to 1.0) at a temperature of 288.15 K. The model atmosphere consists of 24 homogeneous layers and includes four molecular species: H₂O, CO₂, O₃ and N₂O. Contributions to absorption from lines whose transition frequencies lie up to 25 cm⁻¹ outside the given frequency range are included in the calculation (there are 35,849 lines belonging to the four species in the HITRAN database over this extended frequency range). Monochromatic radiances are calculated at a sampling interval of 0.00114 cm⁻¹ (i.e., at 131,073 sample points). No independent model of continuum absorption or of line-mixing is included. Computations are conducted on a SPARCcenter

1000 with ??? bytes of RAM, under Sun operating system V Release 4.0 and with SPARCompiler C 2.0.1 (computational performance was assessed at times when there were no competing processes executing other than system calls).

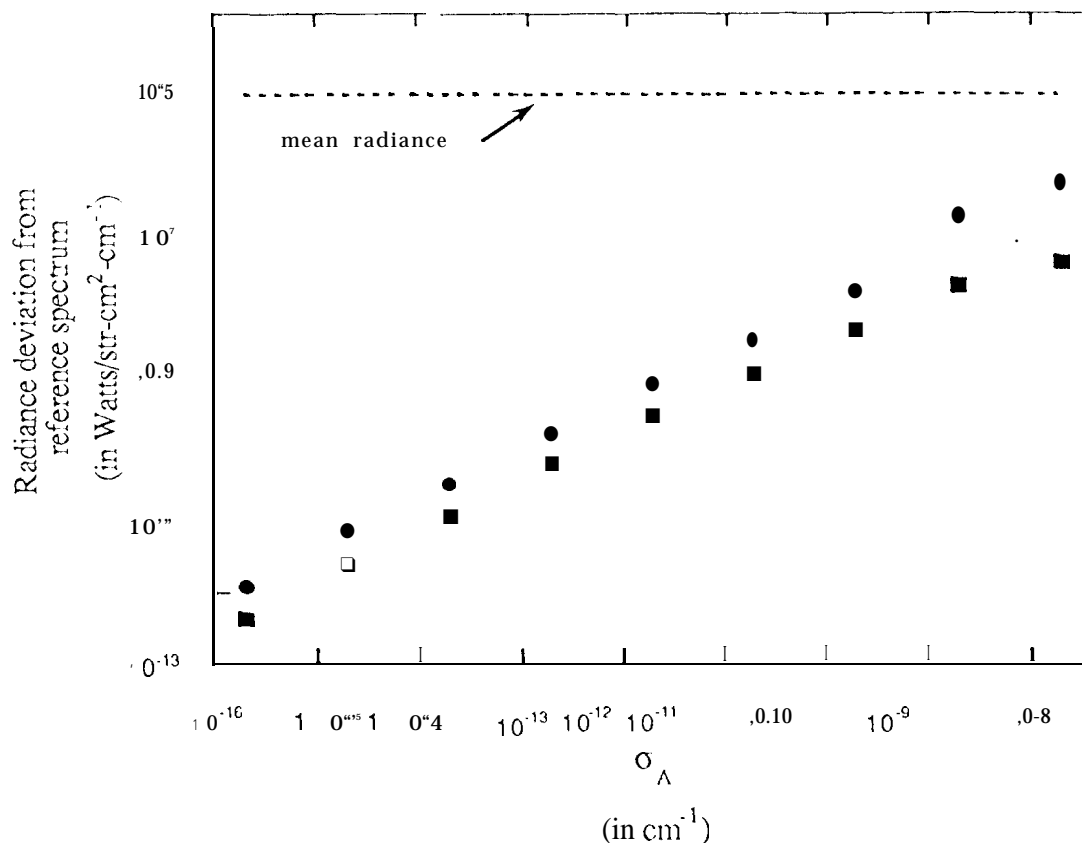


Figure 4. Deviation of calculated benchmark radiances from their corresponding values in the reference spectrum vs. the magnitude of the line accuracy coefficient. The squares and circles represent, respectively, the mot mean square deviation and maximum deviation. The value of (he mean radiance of the spectrum is also indicated. All lines in the HITRAN database belonging to the four benchmark species over the extended range 625-825 cm^{-1} have been included in the calculations.

The numerical error associated with neglecting terms in the summation of eq. (5) can be made arbitrarily small according to the specified value of the line accuracy coefficient σ_A . Figure 4 displays the numerical error in the benchmark spectrum that

results from varying this coefficient. The calculated radiances are compared to those of a reference spectrum, and both the root mean square deviation and the maximum deviation are plotted. The reference spectrum has been generated using absorption coefficients calculated in each layer at each grid point according to eq. (3), summing over all the lines in the HITRAN database belonging to the four benchmark species within the extended range 62.5 - 825 cm^{-1} ; in this sense, the reference spectrum represents the exact result that the calculated spectra represented in Fig. 4 strive to approximate accurately. Each spectrum approximating this solution has been generated using absorption coefficients calculated in each layer at 131,070 grid points according to eq. (5), summing over the same 35,849 lines (eq. (3) is used at the three base tier grid points). Figure 4 shows that the calculated spectra converge smoothly to the reference spectrum as σ_A is reduced over several orders of magnitude. For the smallest value of σ_A displayed, the agreement is 7-8 digits at each frequency grid point, and the agreement continues to improve in the same fashion for even smaller values of σ_A .

8. Line Rejection

To evaluate the numerical error associated with neglecting weak lines altogether [*i.e.*, in eq. (3) as well as eq. (5)], we define the line rejection coefficient σ_R such that a given line is omitted from the calculation when the absorption at line center, $\sigma_{s,\ell}(\nu_\ell)$, is less than σ_R . The value of σ_R is set by the user at run time. (Note that, throughout this study, we have used the user-specified values of σ_A and σ_R in each layer of a given calculation; one could equally well specify a critical optical depth for line approximation τ_A and a critical optical depth for line rejection τ_R and define layer-dependent coefficients $\sigma_A = \tau_A / \Delta s$ and $\sigma_R = \tau_R / \Delta s$, where Δs is the layer thickness. This does not significantly alter the results that are presented here - the two formulations are equivalent when using layers of equal thickness.) By specifying, $\sigma_A \ll \sigma_R$, we can study the numerical error that arises solely due to line rejection. Alternatively, we can approach optimal performance by requiring that the error due to line rejection be comparable to the error due to line approximation.

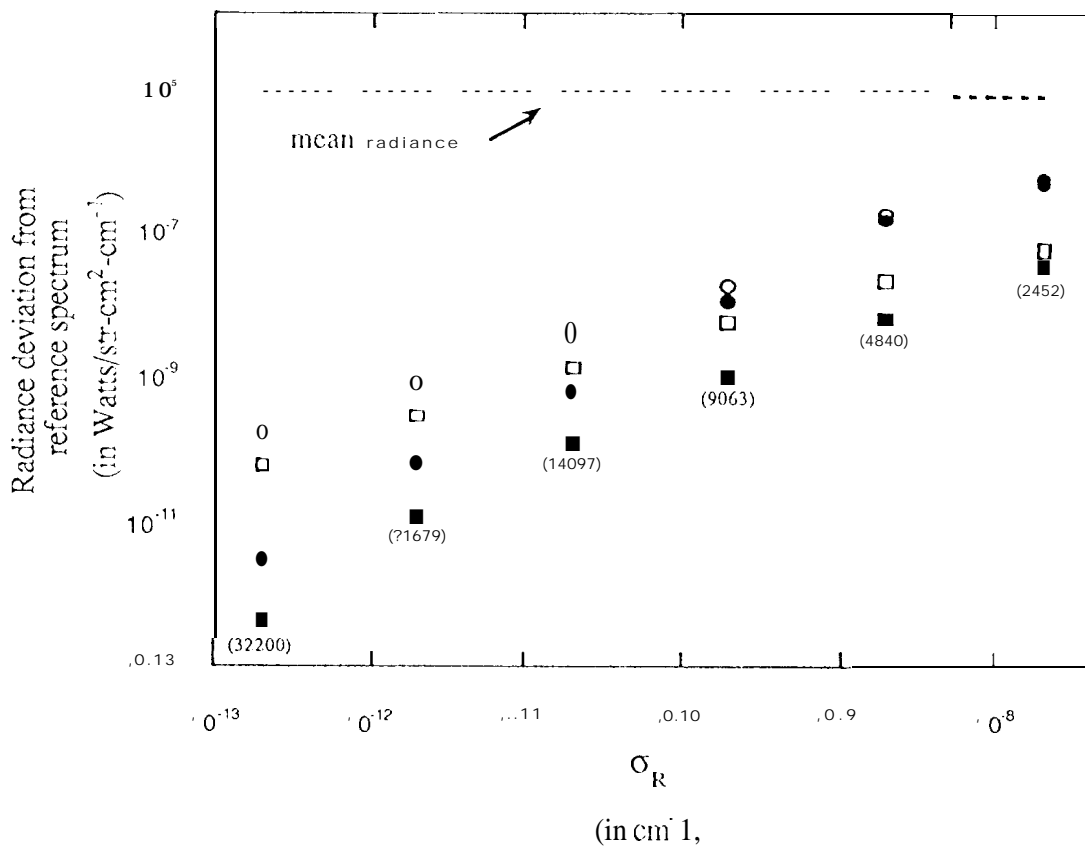


Figure S. Deviation of calculated benchmark radiances from their corresponding values in the reference spectrum vs. the magnitude of the line rejection coefficient. The squares and circles represent, respectively, the root mean square deviation and maximum deviation. Open markers identify spectra where the error is due to both line approximation and line rejection ($\sigma_A = \sigma_R$); solid markers identify spectra where the error is due to line rejection only ($\sigma_A = 10^{-4} \sigma_R$). The value of the mean radiance of the spectrum is also indicated. In parentheses beneath each column of markers is the mean number of lines per layer (out of a possible 35,849) retained in the radiative transfer model for the given value of σ_R .

Figure 5 displays the numerical error that results when σ_R is varied for two sets of spectra: one in which this error is primarily due to line rejection ($\sigma_A \ll \sigma_R$) and one in which the numerical error is due both to line rejection and line approximation ($\sigma_A = O-R$). Calculated values of the benchmark radiances are again compared to their values in the

reference spectrum, and both the root mean square deviation and the maximum deviation are plotted. Also displayed are the number of lines (out of a possible 35,849 lines) retained in the calculation for each value of σ_R . Both sets of calculated spectra converge smoothly to the reference spectrum as σ_R is reduced over several orders of magnitude.

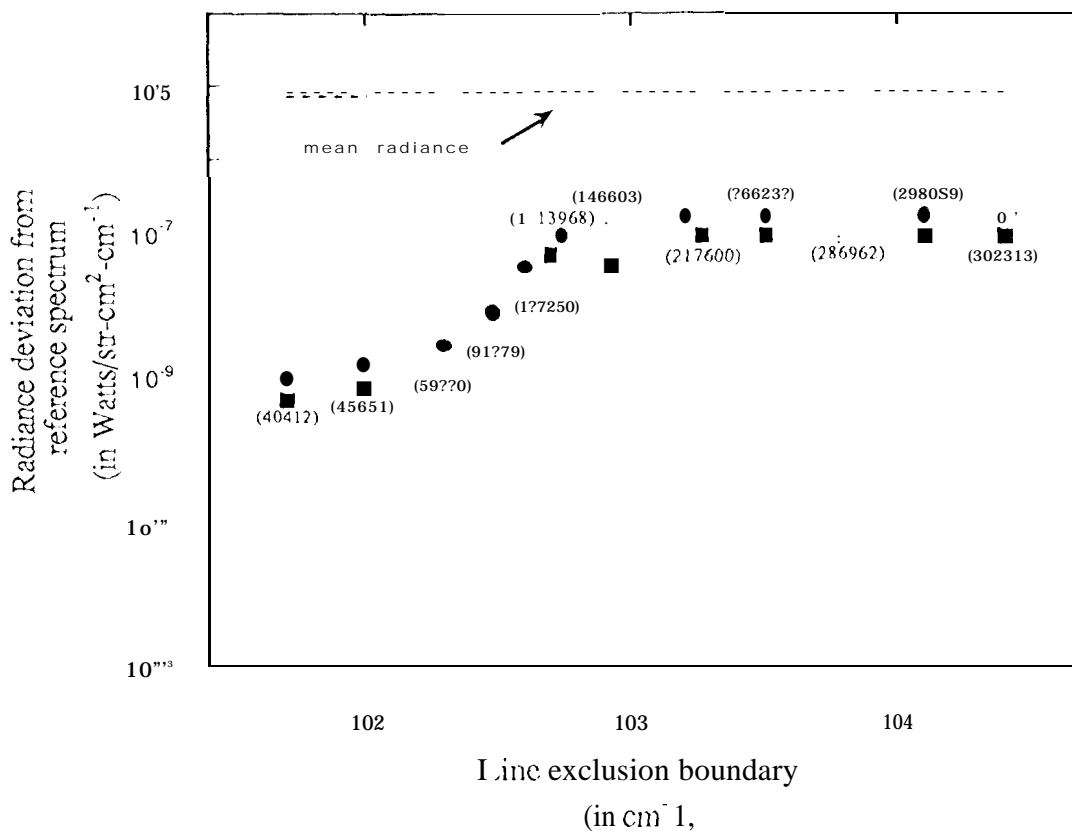


Figure 6. Deviation of benchmark radiances from their reference values vs the magnitude of the line exclusion boundary. The squares and circles represent, respectively, the root mean square deviation and maximum deviation of calculated radiances from their corresponding values in the reference spectrum. The value of the mean radiance of the reference spectrum is also indicated. In parentheses near each pair of markers is the number of lines (out of a possible 303,213) retained in the radiative transfer model for the given exclusion boundary.

in all calculations discussed thus far (including the calculation of the reference spectrum), the *line exclusion boundary*, defined as the distance from the boundaries of the frequency range of interest beyond which spectra lines are automatically excluded from

the radiative transfer model, has been set equal to 25 cm^{-1} . The numerical error that results from the exclusion of lines beyond this boundary can be inferred from Fig. 6, where, we have increased the magnitude of the line exclusion boundary and compared the calculated values of the benchmark radiances to their values in the reference spectrum, plotting the root mean square deviation and the maximum deviation. In these calculations, we have set $\sigma_R = 0$, and we have required σ_A to be sufficiently small such that the error due to line approximation is negligible compared to the effect of including more, increasingly distant lines in the calculation. In parentheses near each pair of markers is displayed the number of lines retained in the radiative transfer model for the given exclusion boundary (note that there are a total of 302,213 lines belonging to the four benchmark species represented in the 1992 HITRAN database). The inclusion of more distant lines in the radiative transfer model has negligible impact for this particular frequency range once the exclusion boundary exceeds 1000 cm^{-1} .

9. Efficiency

By plotting the time of program execution as a function of the line accuracy coefficient σ_A , we may assess the relative computational cost of achieving increasingly higher numerical accuracy. Fig. 7 displays the execution time required to generate two sets of spectra discussed previously: one with $\sigma_R = 0$ (corresponding to the spectra represented in Fig. 4) and one with $\sigma_R = \sigma_A$ (corresponding to the spectra represented by open markers in Fig. 5). In this figure, execution time is defined as the sum of the *user* and *system* CPU time as reported by the UNIX *time* utility. To distinguish the time devoted to the calculation of absorption coefficients from the time required (1) to initialize the observational model, (2) to read and sort linelist entries over the frequency range of interest, (3) to perform the radiative transfer integration, and (4) to handle the data input and output, we have determined the latter by repeating the spectral calculation substituting zeros for all absorption coefficients rather than calculating them. The result is designate.ci "overhead" in Fig. 7.

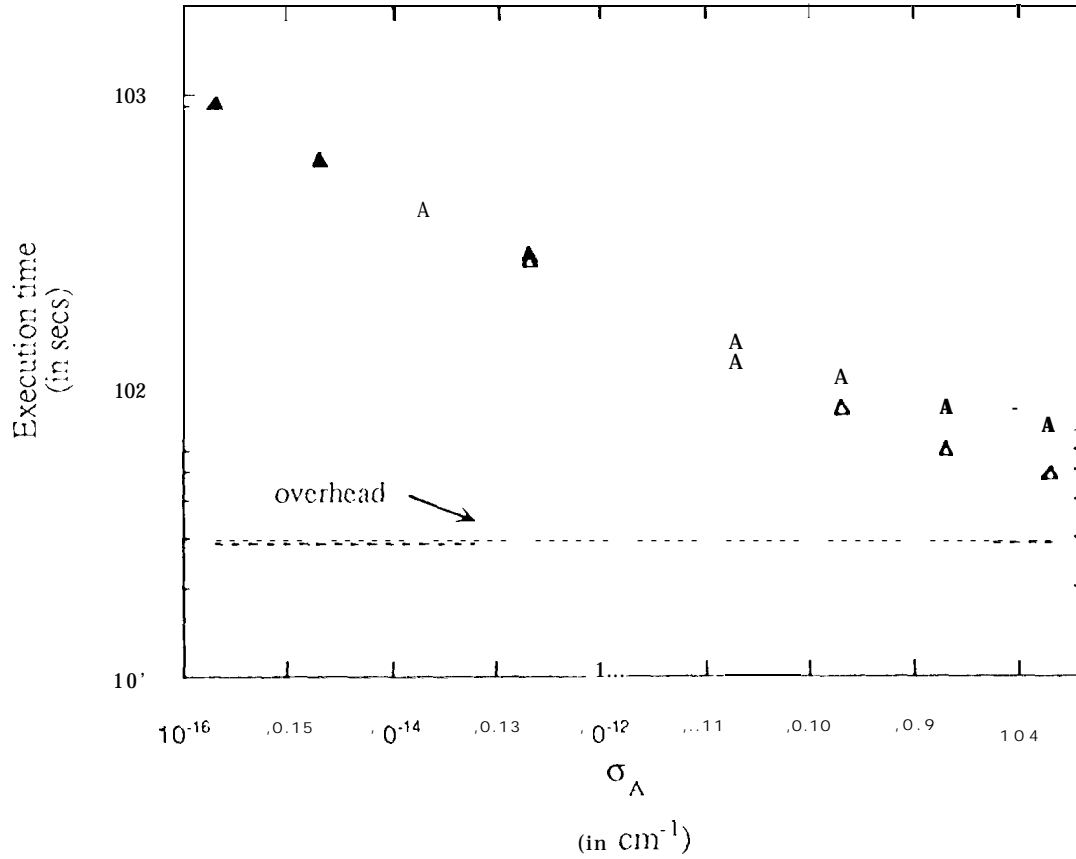


Figure 7. Execution time vs. the magnitude of the line accuracy coefficient. Solid triangles indicate spectra calculated with $\sigma_R = 0$; open triangles indicate spectra calculated with $\sigma_R = \sigma_A$. Also indicated is the execution time required for "overhead", *i.e.*, the time required to initialize the observational model, to read and sort line list entries, to model the radiative transfer, and to handle input and output, but exclusive of the time required to calculate absorption coefficients.

The execution time required to compute the reference spectrum is 3.81×10^5 seconds (*i.e.*, more than four days). This is larger than the execution time required to compute the spectrum at $\sigma_A = 2.0 \times 10^{-16}$ by more than a factor of 400. Performance improves by an additional order of magnitude at larger values of σ_A . Comparing Fig. 4 and Fig. 7, we find that each order-of-magnitude reduction in the numerical error requires less than a factor of two increase in the execution time.

The efficiency of the method of approximation is achieved by minimizing the number of points at which each line profile is evaluated, in a manner consistent with the degree of numerical accuracy sought. The mean number of points evaluated per line in a given layer is a function of both the line accuracy coefficient and the line rejection coefficient. Figure 8 shows the mean number of points evaluated per line in the first layer of the benchmark calculation for the same spectra as represented in Fig. 7. The maximum number of points evaluated for any line is also plotted (which, of course, is independent of σ_R).

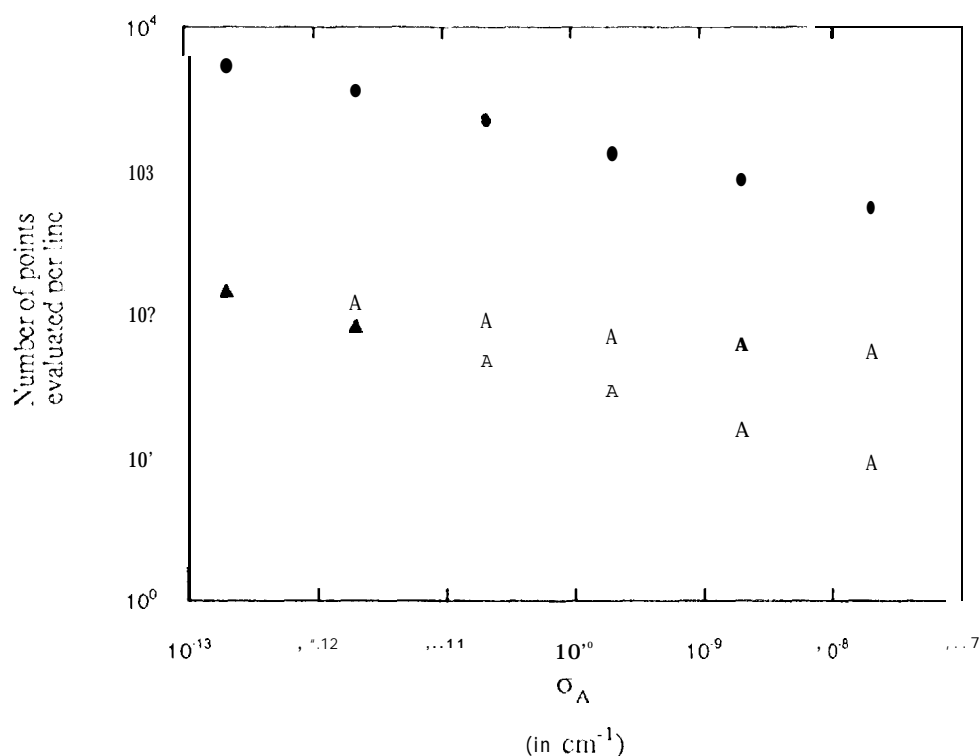


Figure 8. Number of points evaluated per line in the first layer of the benchmark calculation vs. the magnitude of the line accuracy coefficient. Solid triangles indicate the mean number of points evaluated per line when $\sigma_R = 0$. Open triangles indicate the mean number of points evaluated per line when $\sigma_R = \sigma_A$. Circles indicate the maximum number of points evaluated for any line.

Note first that, for all values of σ_A , the maximum typically differs from each mean by more than an order of magnitude; *i.e.*, there are a few strong lines that are

calculated much more precisely than the average line. For fixed σ_A , the mean number of points evaluated per line increases as σ_R increases, *since* increasing σ_R eliminates weak lines altogether that would otherwise each be evaluated at fewer points than the mean. For fixed σ_R , the mean number of points per line increases as σ_A decreases, since reducing the error due to line approximation requires evaluating more points per line. The magnitude of each mean plotted in Fig. 8 is generally representative of the magnitude of the corresponding mean for each higher layer (the magnitude of each maximum decreases by roughly a factor of two upon reaching the top layer).

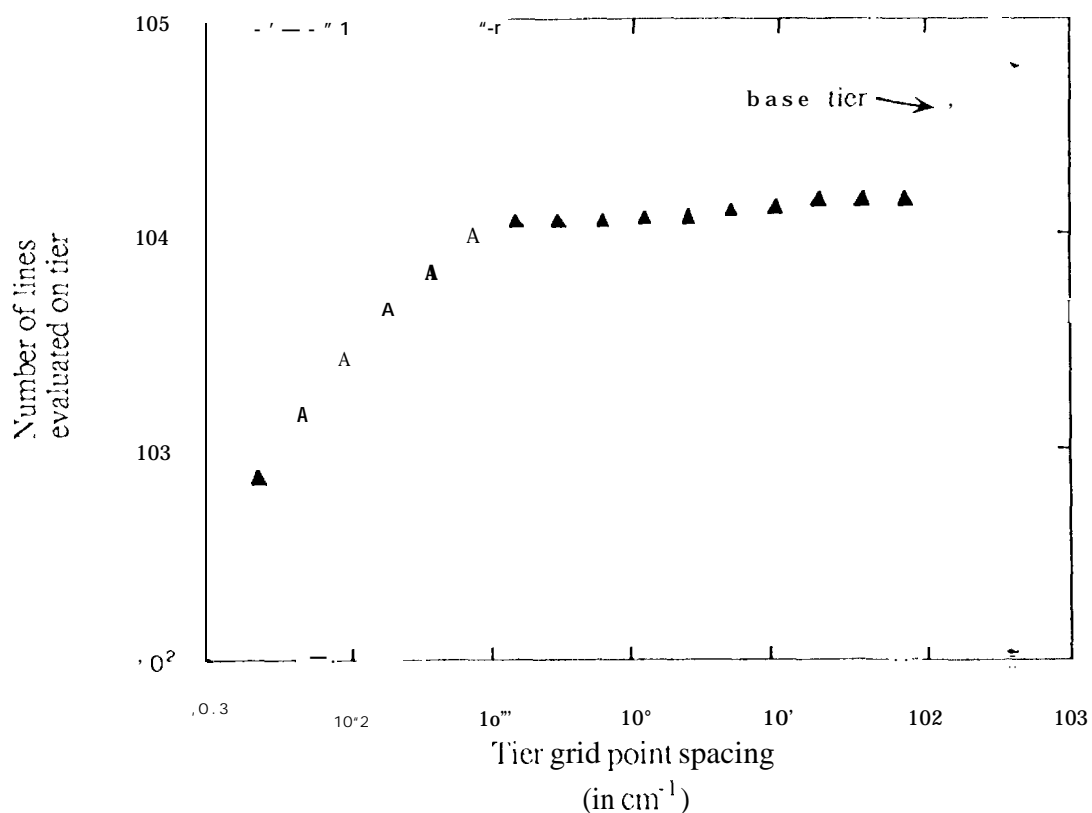


Figure 9. Number of lines evaluated vs. tier (identified by the size of the interval separating its grid points) in the first layer of the benchmark calculation with $\sigma_A = 2.0 \times 10^{-10}$ and $\sigma_R = 0$.

To gain insight into how the execution time is apportioned within the algorithm, it is useful to examine, on a tier-by-tier basis, both the number of lines evaluated in a layer and the number of points evaluated per line. Figure 9 shows the number of lines

evaluated on each tier in the first layer for the benchmark spectrum calculated with $\sigma_A = 2.0 \times 10^{-10}$ and $\sigma_R = 0$. All 35,849 lines are evaluated at the three points in the base tier (in both Figs. 9 and 10, the base tier value is plotted at twice the base tier grid point spacing for clarity, since the grid point spacing in each of the first two tiers is identical). However, a large fraction of these lines are extremely weak, as indicated by the fact that roughly 60% are neglected on the next tier. Then as one moves to higher tiers (*i.e.*, smaller tier grid point spacing), the number of lines per tier changes slowly until, at -0.1 cm^{-1} , the interpolation sampling interval becomes sufficiently fine, that an increasing number of lines can be neglected.

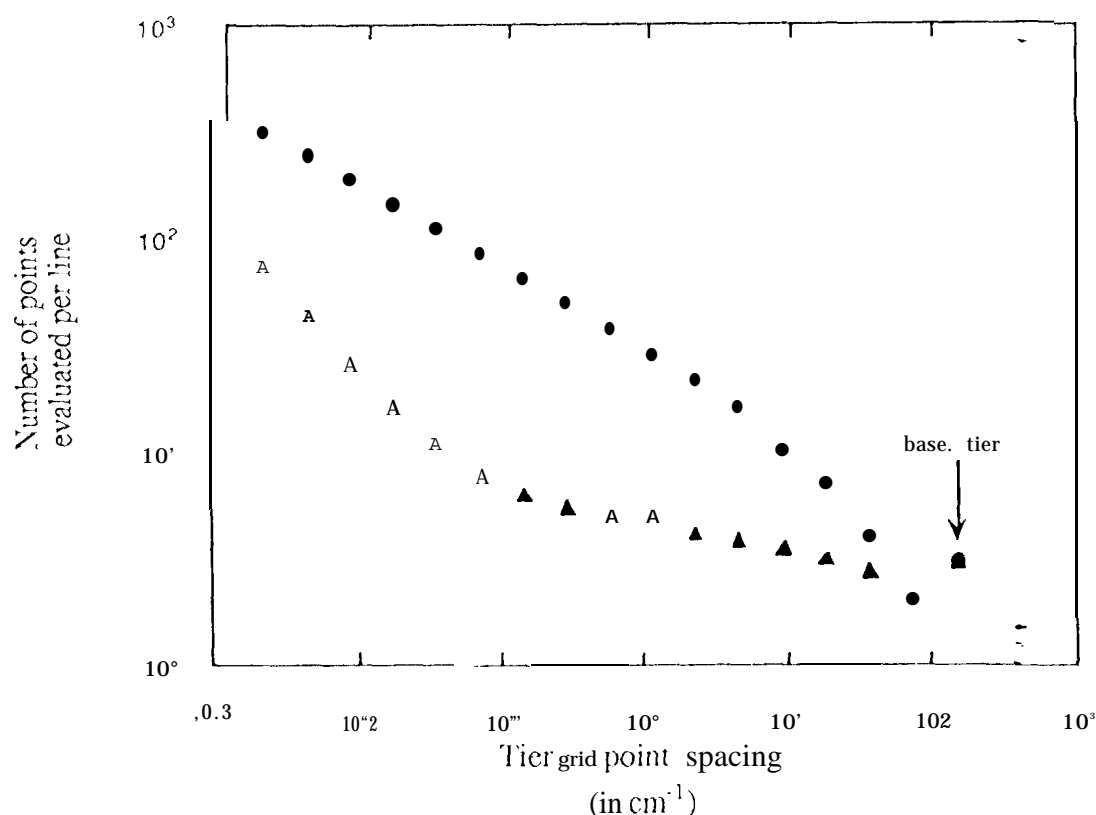


Figure 10. Number of points evaluated per line vs. tier (identified by the size of the interval separating its grid points) in the first layer of the benchmark calculation with $\sigma_A = 2.0 \times 10^{-10}$ and $\sigma_R = 0$. Circles indicate the maximum number of points evaluated for any line. Triangles indicate the mean number of points evaluated per line, where the mean is calculated over only those lines for which one or more points are evaluated on the tier.

Figure 10 displays the number of points per line evaluated on each tier in the first layer for the benchmark spectrum calculated with $\sigma_A = 2.0 \times 10^{-10}$ and $\sigma_R = 0$: the circles indicate the maximum number of points evaluated for any line, and the triangles indicate the mean number of points evaluated per line where each mean is calculated over only those lines for which one or more points are evaluated on the tier (the number of such lines for the tier is indicated in Fig. 9). The product of each ordinate in Fig. 9 and the corresponding mean in Fig. 10 gives the total number of points evaluated in the first layer for that tier. For tiers above the second tier, this product does not vary by more than a factor of two. A similar conclusion obtains as well for layers above the first layer.

in all calculations presented thus far, the frequency interval $650\text{-}800\text{ cm}^{-1}$ has been sampled at 131,073 points. The execution time required to calculate the benchmark spectrum will, of course, decrease as the magnitude of the sampling interval is increased. Figure 11 shows the variation of execution time with the number of sample points, where benchmark spectra are calculated with $\sigma_R = 0\text{-}A$ and $\sigma_A = 2.0 \times 10^{-8}$, 2.0×10^{-9} , and, 2.0×10^{-10} .

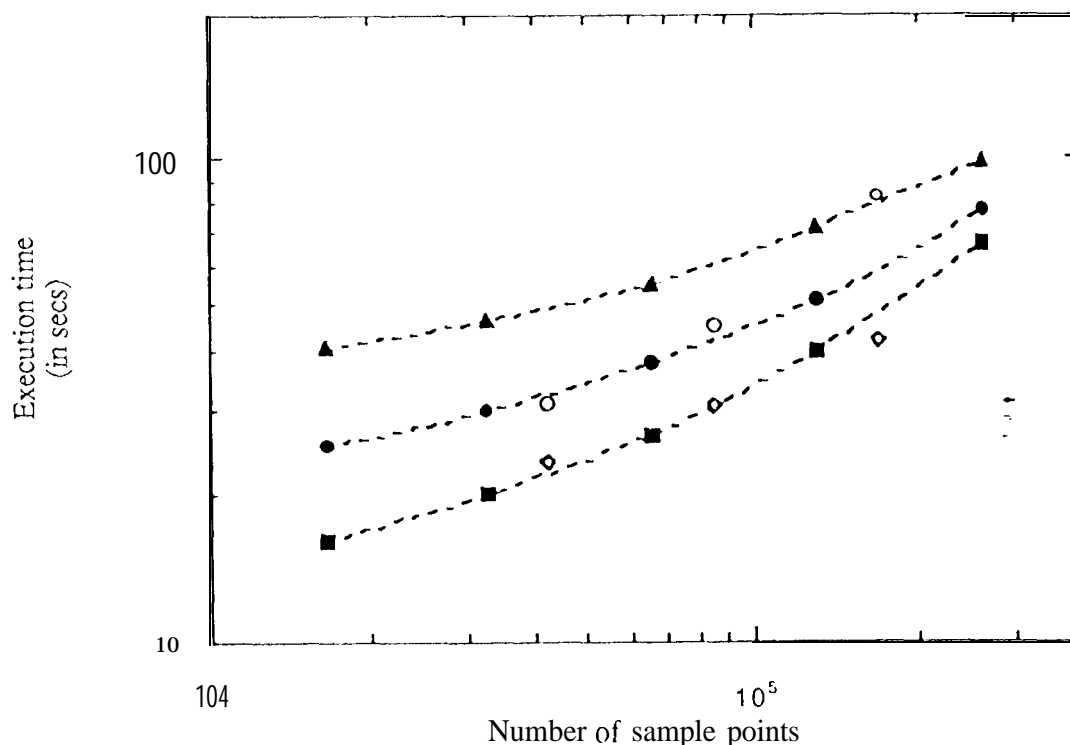


Figure 11. Execution time vs. the total number of spectral sample points in the frequency interval $650\text{--}800\text{ cm}^{-1}$. Solid markers refer to benchmark spectra calculated with

$\sigma_R = \sigma_A$: squares indicate $\sigma_A = 2.0 \times 10^{-8}$; circles indicate $\sigma_A = 2.0 \times 10^{-9}$; triangles indicate $\sigma_A = 2.0 \times 10^{-10}$. Open markers refer to spectra generated by LBLRTM; diamonds indicate DPTMIN = 0.0002 and DPTFAC = 0.001; circles indicate DPTMIN = 0 and DPTFAC = 0. Each curve through solid markers has been plotted to identify a set of solutions with the same numerical accuracy; the numerical error of the LBLRTM solutions varies with the number of sample points.

For purposes of comparison, we have also displayed in Fig. 11 the execution times exhibited by LBLRTM (Clough, 1993) in the same computational environment to produce similar sets of benchmark spectra. LBLRTM is a FORTRAN program designed to achieve high speed (or, more precisely, the highest possible speed consistent with maintaining an accuracy of the order of 0.2% in the monochromatic value of the optical depth). In LBLRTM, we have endeavored to reproduce as closely as possible the observational model of the benchmark described in Section 7 (e.g., we have excluded the continuum model and line-mixing from the LBLRTM calculations). We have employed the companion program LNIL to pre-sort the HITRAN database, using the default line selection criteria. There are two sets of LBLRTM spectra represented in Fig. 11, one with additional, dynamic line rejection (as dictated by setting the input parameters DPTMIN = 0.0002 and DPTFAC = 0.001) and one without additional line rejection (DPTMIN = 0 and DPTFAC = 0). The number of sample points is determined within LBLRTM according to the value of the input parameter SAMPLE (the number of sample points per mean half-width). We have varied SAMPLE over its recommended range of validity, setting it equal to 1.0, 2.0, and 4.0.

In standard operation, SEASCRAPF selects linelist entries from a binary version of the entire HITRAN database. However, to eliminate in Fig. 11 differences in execution time due to the pre-sorting of the HITRAN database, we have run SEASCRAPF using a condensed input linelist comprised of the same set of lines as chosen by LNIL. Thus, the execution times in Fig. 11 for the spectra (with 131,073 sample points) generated by SEASCRAPF are somewhat lower than the execution times for the corresponding spectra presented in Fig. 7.

For inter-code comparison of execution times to be meaningful, we should ensure that the solutions compared possess similar numerical accuracy. By differencing the two LBLRTM solutions comprised of 169,504 sample points, we can determine a lower bound on the numerical error due to line rejection alone: their root-mean-square difference is 1.1×10^{-8} Watts / $\text{str} \cdot \text{cm}^2 \cdot \text{cm}^{-1}$ and the maximum difference is 4.7×10^{-8} Watts / $\text{str} \cdot \text{cm}^2 \cdot \text{cm}^{-1}$. We have made no attempt, however, to quantify the additional numerical error in the LBLRTM solutions due to the analytic model used to approximate the Voigt function nor the interpolation error resulting from the manner in which this analytic model is approximated (the dependence of the numerical error of such spectra on the size of the sampling interval is discussed in Clough and Kneizys [1979]).

As a means of assessing the relative performance of the two approaches to evaluating absorption, comparison of execution times presented in Fig. 11 is less than ideal. Differences in execution time are due not only to the respective methods of calculating absorption coefficients, but also to differences in (1) the initialization of the Observational model, (2) the method of integrating the radiative transfer equation, (3) the manner in which input and output are handled, (4) the relative efficiencies of equivalent C and FORTRAN library routines, etc. It would be preferable to test two codes that differ

only in the modules used to calculate absorption coefficients. All approximate solutions could then be compared to the same reference spectrum. With regard to the codes in question, a rigorous analysis of the differences in their respective approaches to calculating radiative transfer is beyond the scope of this paper.

10. Discussion

In the method of calculating absorption coefficients presented here, numerical accuracy does not depend upon the size of the spectral sampling interval. Indeed, doubling the resolution of a calculation (i. e., halving the magnitude of the sampling interval) does not alter the values of the monochromatic radiances at each sampling frequency shared by the two solutions. Doubling the resolution is achieved simply by creating a new top tier comprised of the midpoints of the sampling intervals for the original solution, and this does not affect the calculation of radiances at frequency grid points belonging to the original set of tiers.

Since the numerical accuracy of the method is independent of the spectral sampling interval, we are free to specify the sampling interval according to other criteria. For example, if we wish to model the response of an observing instrument to incident radiation, the sampling interval can be chosen to achieve a specified accuracy when the monochromatic radiances are convolved numerically with the instrumental apparatus function. Note that the method of approximation may be conveniently used in conjunction with Fast Fourier Transform methods to evaluate such integrals, since both techniques require that the number of sample points be defined in terms of powers of two.

The method of approximation is highly efficient at handling the small but numerous contributions to absorption from the far wings of spectral lines, especially of those lines whose transition frequencies lie outside the frequency range of interest. This capability should be of particular value in validating the accuracy of improved models for the far wings as they become available. (In other forward models (Clough *et al.*, 1981; Edwards, 1988), these far wing contributions to absorption are considered as part of the continuum (Clough *et al.*, 1989); it should be noted that the LBLRTM continuum model can be implemented in conjunction with the method of calculating absorption coefficients presented here). When a line is sufficiently weak or when its transition frequency lies sufficiently far from the boundaries of this frequency range, the contribution of the line to absorption at all frequency grid points within this range may be included by evaluating the line profile at only the grid points of the base tier. It is thereby possible to calculate efficiently and accurately the small corrections to computed radiances arising from the superposition of thousands of extremely small contributions to absorption from the far wings of spectral lines. For example, the execution time required to calculate the spectrum of Fig. 6 with 303,213 lines in the radiative transfer model differs from the execution time required to calculate the spectrum with 35,849 lines by only a factor of ??? when $\sigma_A = 2.0 \times 10^{-8}$ and the linelist is pre-sorted.

The method of approximation may be readily generalized to apply to more sophisticated line shape models or to accommodate different line shape factors for different molecular species. In general, using a different line shape model will require defining a new table of cutoffs analogous to the Lorentz cutoffs discussed in Section 3. Implementation of line-mixing in CO₂, for example, requires defining a separate table of cutoffs since the line shape function decays asymptotically as $|\nu - \nu_l|^{-1}$ rather than

$|v - v_L|^{-2}$ (Edwards and Stew, 1991). In practice, however, it may often prove sufficient to continue to use the Lorentz cutoffs, especially when the line shape model consists of a Lorentzian profile modified by a corrective factor χ (often χ takes the form of a decaying exponential with adjustable coefficients determined empirically). The validity of using the Lorentz cutoffs can be readily established by a convergence study similar to that presented in Fig. 4.

We have implemented the approximation algorithm within SEASCAPE using three-point Lagrangian interpolation. The question arises whether the use of higher order interpolation might lead to improved performance. The advantage of using higher orders of interpolation is that generally fewer points per line need to be evaluated to achieve a given level of accuracy. On each tier with relatively fine spacing ($\Delta v \leq \alpha_{L,t}$), the Lorentz cutoff for a given line may become significantly smaller. For example, by plotting the equivalent of Fig. 2 for five-point Lagrangian interpolation, we find that the number of points that need to be evaluated on a given tier to achieve a given level accuracy can be reduced by up to an order of magnitude. The advantages of using lower orders of interpolation are three-fold: (1) the evaluation of each interpolation is less expensive since it involves fewer terms; (2) the base tier can be comprised of fewer points (note: the base tier must be constructed to have, at least as many grid points as the order of the interpolation scheme; e.g., to use four or five-point Lagrangian interpolation, the first two tiers of Fig. 1 should be combined to form a single tier with five points); (3) fewer points need to be evaluated on each tier with relatively coarse spacing ($\Delta v \gg \alpha_{L,t}$), to achieve a given level of accuracy (according to the definition of the Lorentz cutoff in Section 3, the magnitude of $\xi_{L,t}(\Delta v, \alpha_{L,t})$ on such a tier will always exceed a value which is one less than the order of interpolation).

In a limited set of studies substituting four-point interpolation for three-point interpolation, we have found that the advantages and disadvantages roughly compensate producing no significant improvement in performance. However, the algorithm for calculating absorption coefficients does not require that the same order of interpolation be used on all tiers within all layers, only that the same order of interpolation be used consistently on the same tier within a given layer. Thus, it is likely that optimal performance may require using lower order interpolation on lower tiers and higher order interpolation on higher tiers. We have not attempted to quantify the improvement in performance that such an implementation would attain.

To perform atmospheric retrievals, it is necessary to calculate not only the absorption coefficients but also their partial derivatives with respect to each parameter being retrieved. By differentiating eq. (5) with respect to a retrieved parameter, we may use the same algorithm to calculate the partial derivative of an absorption coefficient as is used to calculate the coefficient itself.

11. Conclusion

This paper has presented an efficient method for calculating spectral absorption coefficients on a line-by-line basis to arbitrarily high numerical accuracy. The method is conceptually simple and may be readily applied to any analytic model for the spectral line shape. Numerical accuracy is continuously adjustable over many orders of magnitude and, unlike other line-by-line forward models, this accuracy is independent of the size of the interval with which the spectrum is sampled.

By decoupling the numerical accuracy from the sampling interval, this method provides additional opportunities for optimizing the retrieval of atmospheric profiles. One may anticipate that, during the initial iterations of the retrieval process, relatively low accuracy and coarse sampling may be used to obtain quickly a sequence of approximate solutions of increasing accuracy. As convergence is approached, both the permitted level of error and the size of the sampling interval can be reduced continuously to attain the desired solution.

Acknowledgments

Portions of [his work were carried at the Jet Propulsion Laboratory, California institute of Technology, under contract with the National Aeronautics and Space Administration.

References

- Armstrong, B. H., Spectrum line profiles: the Voigt function, *J. Quant. Spectrosc. Radiat. Transfer* **7**, 66 (1967).
- Clough, S. A., Radiative Transfer Model Development in Support of the Atmospheric Radiation Measurement Program, *Proceedings of the 3rd Atmospheric Radiation Measurement (ARM) Science Team Meeting, CONF-9303112*, Norman, OK, 1993.
- (Clough, S. A., F. X. Kneizys, and R. W. Davies, "Line shape and the water vapor continuum", *Atmospheric Research* **2**, 229 (1989).
- (Clough, S. A., and F. X. Kneizys, *Appl. Opt.* **18**, 2329 (1979).
- Clough, S. A., F. X. Kneizys, L. S. Rothman, and W. O. Gallery, *SPIE Proc.* **277**, *Atmospheric Transmission*, 152 (1981).
- Drayson, S. R., *Appl. Opt.* **5**, 385 (1966).
- Edwards, D. P., *SPIE Proc.* **298**, Modeling of the Atmosphere, 1 (1988).
- Edwards, D. P. and L. L. Strew, *J. Geophys. Res.* **96**, 20859 (1991).
- Fomin, B. A., *J. Quant. Spectrosc. Radiat. Transfer* **53**, 663 (1995).
- Gamache, R. R., R. L. Hawkins, and L. S. Rothman, *Journal of Molecular Spectroscopy* **142**, 205-219 (1990).
- Goody, R. M. and Y. L. Yung, *Atmospheric Radiation - Theoretical Basis* (Oxford University Press: Oxford, 1989).
- Kary, A. I. *J. Quant. Spectrosc. Radiat. Transfer* **20**, 379 (1978).
- Kunde, V. G. and W. C. Maguire, *J. Quant. Spectrosc. Radiat. Transfer* **14**, 803 (1974).
- Rodgers, C. D., *J. of Geophys. Res.* **95**, S587 (1990).
- Rothman, L. S., R. R. Gamache, R. H. Tipping, C. P. Rinsland, M. A. H. Smith, D. Chris Benner, V. Malathy Devi, J.-M. Flaud, C. Camy-Peyret, A. Perrin, A. Goldman, S. "P". Massie, L., R. Brown, and R. A. Toth, *J. Quant. Spectrosc. Radiat. Transfer* **48**, 479 (1992).

- Schreier, F., The Voigt and complex error function; a comparison of computational methods, *J. Quant. Spectrosc. Radiat. Transfer* **48**, 743 (1992).
- Scott, N. A., *J. Quant. Spectrosc. Radiat. Transfer* **14**, 691 (1974).
- Smith, H. J. P., D. J. Dube, M. E. Gardner, S. A. Clough, F. X. Kneizys, L. S. Rothman, FASCODE-Fast Atmospheric Signature Code (Spectral Transmittance and Radiance), AFGL-TR-78-0081, 1978.
- Sparks, L., "Accelerated line-by-line calculation of spectral absorption coefficients with high numerical accuracy", in *Optical Remote Sensing of the Atmosphere*, Vol. 2, 1995 OSA Technical Digest Series, pp. 68 - 70 (Optical Society of America, Washington, DC, 1995).
- Sparks *et al.*, 1996, manuscript in preparation.
- Susskind, J. and J. E. Sear, *JQSRT* **19**, 195 (1978).
- Turner, D. S., *J. Quant. Spectrosc. Radiat. Transfer* **53**, 633 (1995).
- Uchiyama, A., *J. Quant. Spectrosc. Radiat. Transfer* **47**, 521 (1992).

Appendix

This Appendix describes in greater detail the behavior of $\delta g_p(z, \Lambda z)$ as defined in eq. (1.3). Expanding each function on the right hand side of eq. (1.1) about z for $\Lambda z \ll |z|$,

$$\delta g_p(z, \Lambda z) \approx \frac{\Lambda z^3}{6} \left| p(1-p^2) \frac{\partial^3 g(z)}{\partial z^3} \right|, \quad (A1)$$

or, after substituting for the third derivative of $g(z)$,

$$\delta g_p(z, \Lambda z) \approx 4\Lambda z^3 \left| p(1-p^2) \frac{z(1-z^2)}{(z^2-1)^3} \right| \quad (A2)$$

Thus, for $|z| \gg 1$ in Fig. 2, $\delta g_p(z, \Lambda z) \sim \Lambda z^3 / |z|^5$ and, along a contour of fixed $\delta g_p(z, \Lambda z)$, $\log_{10} \left| \frac{z}{\Lambda z} \right| = -\frac{2}{5} \log_{10} \Lambda z$. Similarly, for $|z| \ll 1$, $\delta g_p(z, \Lambda z) \sim |z| \Lambda z^3$ and, along a contour of fixed $\delta g_p(z, \Lambda z)$, $\log_{10} \left| \frac{z}{\Lambda z} \right| = -4 \log_{10} \Lambda z$. Notice that as z becomes large, the right hand side of eq. (A2) vanishes much more rapidly ($\sim |z|^{-5}$) than $g(z)$ ($\sim |z|^{-2}$); thus, at frequencies increasingly distant from line center, a term in the summation of eq. (5) will become negligible long before the corresponding term in the summation of eq. (3).

